**Proceedings of the 28th IEEE**
**EMBS Annual International Conference**
**New York City, USA, Aug 30-Sept 3, 2006**



# Detecting false vessel recognitions in retinal fundus analysis

A. Giani, E. Grisan, M. De Luca, A. Ruggeri

***Abstract*—**Automatic tracking of blood vessels in images of retinal fundus is an important and non-invasive procedure for the diagnosis of many diseases. Tracking techniques often present a high rate of false positives. This paper presents six methods to discriminate false detections from true positives, each based on a different model of the vessel. They describe a candidate vessel in terms of its average geometric and grayscale properties considered along the full trajectory of the vessel itself. The rationale is that false vessels are caused by the small scale of the tracking algorithm necessary during the tracking phase. Once tracking has been completed, we can gather information from the full vessel trajectory and solve ambiguities that cannot be fixed during tracking. We apply Fisher linear discriminant analysis to these features to get the desired discrimination. Results on 28 images show satisfactory rejection of false positives and better results when using more complex models.

## I. Introduction

AUTOMATIC tracking of blood vessels in images of retinal fundus is an important and non-invasive procedure for the diagnosis of many diseases. Tracking techniques [1-3] often present a high rate of false positives. False trackings can be generated by choroidal vessels running below the retina producing ghost paths through the partially opaque retinal tissue, or by vessel-like structures caused by hemorrhages or exhudates, or by random paths on the fundus pigmentation. Figure 1 shows a tracking example and a detail showing an high number of false positives.

This problem is more severe when image contrast is poor. In this case it is necessary to reduce the tracking threshold (i.e. the minimum contrast to allow detection) and this may result in an unacceptable amount of false detections. Worse yet, these artifacts are often comparable in caliber and length to true vessels. This paper presents six methods to discriminate false detections from true positives.

## II. Materials

28 retinal images are considered for the experiments. Field of view is 50° and resolution is 1370x1145 pixel. Images include healthy cases as well as pathological ones with exhudates, cotton spots and emorrhages. Luminance and contrast drifts are removed using a normalization method we developed [4]. This pre-processing step also ensures uniform inter-images contrast and luminosity.

We have then applied a classification-based sparse tracking algorithm [3] in order to obtain the desired detection of the retinal network.

Vessel networks in these images have been manually classified so that ground truth is available for training and evaluation. Therefore, by comparing the automatic tracking against the ground truth provided we were able to partition the tracked vessels into true vessels and false positives, to extract the features to be fed to the detection algorithm.

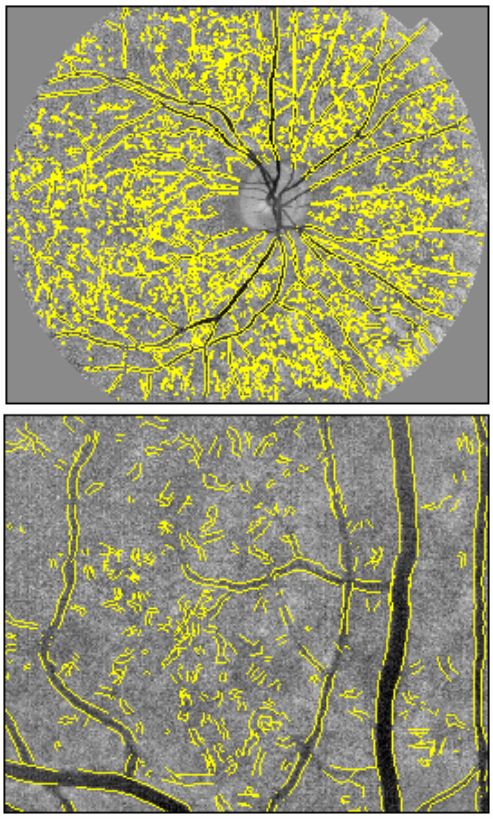

Fig. 1. Vessel tracking in a retinal fundus image (top). Cluster of false positives (bottom)

## III. Methods

False positives are very similar to true vessels when observed locally. However, their non-vessel nature appears evident when the whole vessel is considered. Tracking algorithms follow vessel trajectories typically using small observation windows (figure 2) in order to neglect curvature. This results in a large number of false positives. Grayscale and geometric features can be used to define a classification problem that can be solved using a discriminant analysis.

Manuscript received April 24, 2006.
† Department of Information Engineering, University of Padua, Italy.
Corresponding author: A. Ruggeri, alfredo.ruggeri@unipd.it.

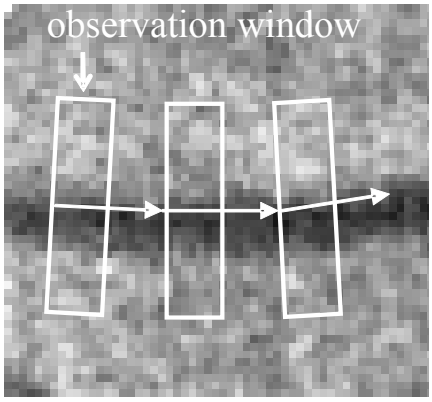


Fig. 2. Tracking algorithm observation window. Limited depth is necessary to model vessel borders as straight lines.

### A. Features selection

The most obvious features are those related to the luminosity (mean) and contrast (variance) of the vessel and of its local background. We define $A^{int}$ the area of image delimited by two vessel borders, and $A^{ext}$ as the background area close to the vessel (figure 3). Internal and external average luminosity and contrast are defined as

$$L^{int} = \frac{1}{area\left(A^{int}\right)} \cdot \sum_{x,y \in A^{int}} p(x,y)$$
$$L^{ext} = \frac{1}{area\left(A^{ext}\right)} \cdot \sum_{x,y \in A^{ext}} p(x,y) \quad (1)$$

$$C^{int} = \frac{1}{area\left(A^{int}\right)} \cdot \sum_{x,y \in A^{int}} \left(p(x,y) - L^{int}\right)^2$$
$$C^{ext} = \frac{1}{area\left(A^{ext}\right)} \cdot \sum_{x,y \in A^{ext}} \left(p(x,y) - L^{ext}\right)^2 \quad (2)$$

where $p(x,y)$ is the grayscale value of the pixel at $x$, $y$. For an ideal vessel $L^{ext} > L^{int}$.

The cross-section of a vessel however follows a Gaussian-like profile[5]. The 2-level model poorly accounts for vessel borders. Silverwire effect (i.e. light reflexion along vessel trajectory due to high reflectance of the vessel walls) also requires more complex models in order to be accounted for. The model is therefore extended by adding a third area, the transition (crossing) area $A^{cross}$, and the corresponding luminosity and contrast features

$$L^{cross} = \frac{1}{area\left(A^{cross}\right)} \cdot \sum_{x,y \in A^{cross}} p(x,y) \quad (3)$$

$$C^{cross} = \frac{1}{area\left(A^{cross}\right)} \cdot \sum_{x,y \in A^{cross}} \left(p(x,y) - L^{cross}\right)^2 \quad (4)$$

Intutively, $L^{int} < L^{cross} < L^{ext}$, as $A^{cross}$ has pixels from both vessel and non-vessel. For the same reason one expects higher contrast $C^{cross}$ compared to $C^{int}$, $C^{ext}$.

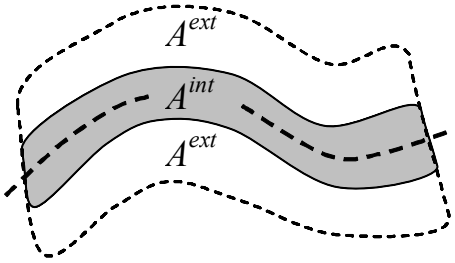


Fig. 3. The simplest model divides the vessel neighborhood in an internal and external area. The asymmetric model considers an upper and lower external area.

This model can be further extended to 4 levels by dividing the cross-section in its internal and external parts with respect to the vessel border, respectively $A^{cross}{}_{i}$ and $A^{cross}{}_{e}$. Furthermore, symmetry can be removed by splitting the upper and lower areas with respects to the vessel axis and having corresponding independent features. Upper and lower features are indicated by subscripts u and *l*. Figure 4 shows a schematic diagram of the 3- and 4-level asymmetric models.

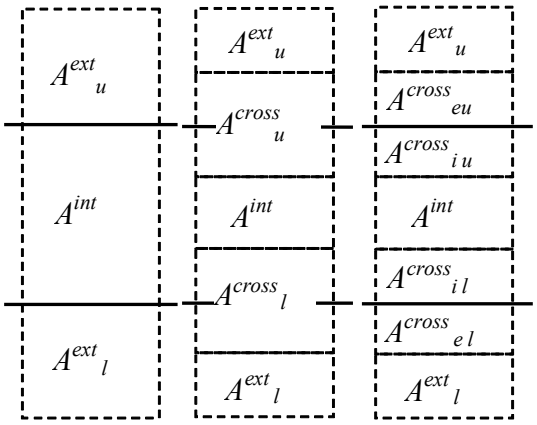


Fig. 4. Left to right: 2-, 3- and 4-areas asymmetric vessel models. Full lines correspond to vessel borders.

Care must be taken in preserving useful information when extending the model. Symmetric external/cross features may provide useful information about texture and structure when combined with their asymmetric counterparts. Symmetric contrast features cannot be computed from the asymmetric ones, therefore they must be included in the feature vector when the model is changed. Accordingly, 3-level cross-

contrast must be included in the 4-level model feature vector, and four cross-contrast features must be added in the 4-level asymmetric model.

Some relationship can be inferred between vessel contrast and caliber [5,6] and therefore it is reasonable to consider the average vessel caliber $\mu_\Delta$ as a parameter. Caliber variance $\Sigma_\Delta$ detects any excess variability in caliber that may point out an artifact. Finally, vessel length may improve artifact rejection since many false vessels are short-lengthened. Table I shows the gray scale features vector $\phi$ for the 6 models considered. Caliber mean and variance and vessel length are included in all models and not shown in table I for simplicity.

TABLE I
VESSEL MODELS AND GRAY SCALE FEATURES VECTOR $\phi$

| 2-zones symm | 2-zones asymm | 3-zones symm | 3-zones asymm | 4-zones symm | 4-zones asymm |
|---|---|---|---|---|---|
| $L^{int}$ | $L^{int}$ | $L^{int}$ | $L^{int}$ | $L^{int}$ | $L^{int}$ |
| $L^{ext}$ | $L^{ext}{}_u$ | $L^{cross}$ | $L^{cross}{}_u$ | $L^{cross}{}_i$ | $L^{cross}{}_{iu}$ |
| $C^{int}$ | $L^{ext}{}_i$ | $L^{ext}$ | $L^{cross}{}_l$ | $L^{cross}{}_e$ | $L^{cross}{}_{eu}$ |
| $C^{ext}$ | $C^{int}$ | $C^{int}$ | $L^{ext}{}_u$ | $L^{ext}$ | $L^{cross}{}_{il}$ |
| | $Cext$ | $C^{cross}$ | $L^{ext}{}_l$ | $C^{int}$ | $L^{cross}{}_{el}$ |
| | $C^{ext}{}_u$ | $C^{ext}$ | $C^{int}$ | $C^{cross}{}_i$ | $L^{ext}{}_u$ |
| | $C^{ext}{}_l$ | | $C^{cross}$ | $C^{cross}{}_e$ | $L^{ext}{}_i$ |
| | | | $C^{cross}{}_u$ | $C^{ext}$ | $C^{int}$ |
| | | | $C^{cross}{}_l$ | | $C^{cross}$ |
| | | | $C^{ext}$ | | $C^{cross}{}_i$ |
| | | | $C^{ext}{}_u$ | | $C^{cross}{}_e$ |
| | | | $C^{ext}{}_l$ | | $C^{cross}{}_u$ |
| | | | | | $C^{cross}{}_l$ |
| | | | | | $C^{cross}{}_{iu}$ |
| | | | | | $C^{cross}{}_{eu}$ |
| | | | | | $C^{cross}{}_{il}$ |
| | | | | | $C^{cross}{}_{el}$ |
| | | | | | $C^{ext}$ |
| | | | | | $C^{ext}{}_u$ |
| | | | | | $C^{ext}{}_l$ |

### B. Vessel classification

Once the vector $\phi$ of features is determined, manually classified data are used to train the linear discriminant w

$$w: \begin{cases} w^T\phi + w_{th} > 0 \Rightarrow \phi \in vessel \\ w^T\phi + w_{th} < 0 \Rightarrow \phi \in non-vessel \end{cases} \quad (5)$$

where $w_{th}$ is the threshold parameter. Linear discriminant is trained according to the Fisher discriminant method [6], which ensures optimal linear separation between the two sets of features by seeking the direction that minimizes inter-class cross-variance (i.e. the amount of overlap between two classes).

## IV. RESULTS

Vessel tracking was applied to the 28 images. Table II shows the false vessel ratio expressed as

$$\rho = \frac{length(false\ vessels)}{length(false\ vessels) + length(true\ vessels)} \quad (6)$$

One can see that on average 50% of each tracking is made of false vessels. The proposed methods aim to reduce this figure.

Two parameters are proposed to measure the performance of the false vessel detection algorithm. Sensibility $\sigma$ measures the ratio between the total length of the true positives *TP* (false vessels correctly detected) and the total length of the corresponding ground truth *GT* (total number of false vessels, both detected and undetected). Accuracy $\alpha$ measures the ratio between the total length of true positives and the total length of positives, including false positives *FP* (i.e. true vessels detected as false).

$$\sigma = \frac{length(TP)}{length(GT)} \quad (7)$$

$$\alpha = \frac{length(TP)}{length(TP) + length(FP)} \quad (8)$$

The six Fisher discriminants are trained using 14 images (training set), whereas the other ones are used as the validation set. Table III shows average σ and α after the application of the six methods proposed.

TABLE II
TRACKING FALSE VESSEL RATIO

| | *training* | | *validation* | |
|---|---|---|---|---|
| | *mean* | *std* | *mean* | *std* |
| $\rho$ | 0.4746 | 0.0567 | 0.6256 | 0.0734 |

TABLE III
SENSITIVITY AND ACCURACY

| | | | 2-zone | 3-zone | 4-zone |
|---|---|---|---|---|---|
| *training* | $\sigma$ | *Symm* | 0.7319 | 0.7879 | 0.8023 |
| | | *Asymm* | 0.7839 | 0.7515 | 0.7674 |
| | $\alpha$ | *Symm* | 0.9722 | 0.9638 | 0.9637 |
| | | *Asymm* | 0.9848 | 0.9720 | 0.9593 |
| *validation* | $\sigma$ | *Symm* | 0.4940 | 0.6164 | 0.6242 |
| | | *Asymm* | 0.6062 | 0.6160 | 0.6365 |
| | $\alpha$ | *Symm* | 0.9529 | 0.9704 | 0.9736 |
| | | *Asymm* | 0.8995 | 0.9476 | 0.9451 |

Results show an overall good detection of false positives at a marginal cost in terms of discarded true vessels. Increasing model complexity generally increases both sensibility and accuracy. In particular, the 4-level asymmetric model provides the best performance in terms of sensibility, whereas the 3-level asymmetric model shows more uniform performance. Figure 5 shows an application example using the asymmetric models. One can see how adding the cross area in 3-zones model improves performance with respects to the simpler 2-zones model. However, marginal gain is achieved when cross area is further divided (4-zones model).

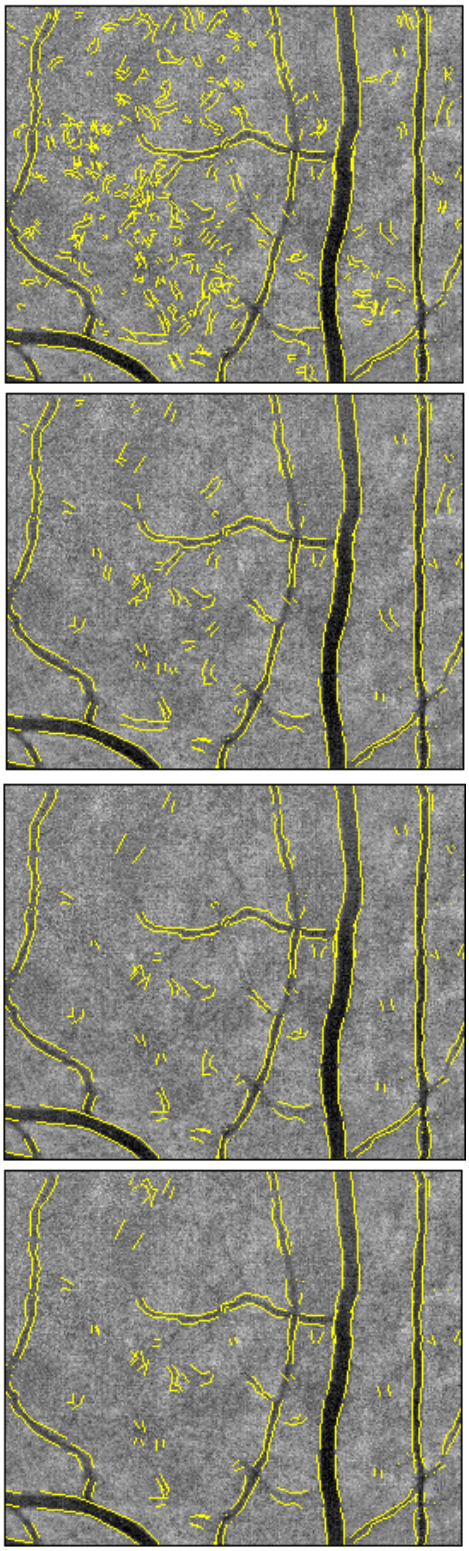

Fig. 5. Top to bottom: source tracking, 2-zones asymmetric, 3-zones asymmetric, 4-zones asymmetric.

## REFERENCES


[1] Tolias Y. A. Panas S. M., "A fuzzy vessel tracking algorithm for retinal images based on fuzzy clustering," *IEEE Transactions on Medical Imaging*, vol. 17, no. 2, pp. 263–273, Mar 1998.

[2] Hoover A., Kouznestova V., Goldbaum M. "Locating blood vessels in retinal images by piece-wise threshold probing of a matched filter response," *IEEE Transactions on Medical Imaging*,, vol. 19, no. 3, pp. 203–210, Mar 2000.

[3] Giani A., Grisan E., Ruggeri A.: "Enhanced Classification-based Vessel Tracking Using Vessel Models and Hough Transform", *3rd EMBEC International Conference*, Prague, Czech Republic, 20-25 Nov 2005.

[4] Foracchia M., Grisan E., Ruggeri A., "Luminosity and contrast normalization in retinal images," *Medical Image Analysis*, vol. 9, n. 3, pp. 179–190, 2005.

[5] Lowell J., Hunter A., Steel D., Basu A., Ryder R., Kennedy R. L. "Measurement of Retinal Vesssel Widths From Fundus Images Based on 2-D Modelling," *IEEE transactions on medical imaging*, vol. 23, no. 10, pp. 1196-1204, Oct 2004.

[6] Leung H. et Al. "Relationships between Age, Blood Pressure, and Retinal Vessel Diameters in an Older Population" *Investigative Ophthalmology & Visual Science*, July 2003, vol. 44, No. 7, pp. 2900-2904, Jul 2003.

[7] Bishop C.M. "Neural Networks for Pattern Recognition," Oxford University Press, 1995.